Influence of Water Content on Speciation and Phase Formation in Zr–Porphyrin-Based MOFs

Charlotte Koschnick, Maxwell W. Terban, Stefano Canossa, Martin Etter, Robert E. Dinnebier, and Bettina V. Lotsch*

Controlled synthesis of phase-pure metal–organic frameworks (MOFs) is essential for their application in technological areas such as catalysis or gas sorption. Yet, knowledge of their phase formation and growth remain rather limited, particularly with respect to species such as water whose vital role in MOF synthesis is often neglected. As a consequence, synthetic protocols often lack reproducibility when multiple MOFs can form from the same metal source and linker, and phase mixtures are obtained with little or no control over their composition. In this work, the role of water in the formation of the Zr–porphyrin MOF disordered PCN-224 (dPCN-224) is investigated. Through X-ray total scattering and scanning electron microscopy, it is observed that dPCN-224 forms via a metal–organic intermediate that consists of $Zr_6O_4(OH)_4$ clusters linked by tetrakis(4-carboxy-phenyl)porphyrin molecules. Importantly, water is not only essential to the formation of $Zr_6O_4(OH)_4$ clusters, but it also plays a primary role in dictating the formation kinetics of dPCN-224. This multidisciplinary approach to studying the speciation of dPCN-224 provides a blueprint for how Zr-MOF synthesis protocols can be assessed and their reproducibility increased, and highlights the importance of understanding the role of water as a decisive component in Zr-MOF formation.

1. Introduction

The formation of metal–organic frameworks (MOFs) relies on coordinative self-assembly of inorganic nodes and organic linkers into periodic coordination networks.[1] The variety of both inorganic and organic building units allows for a wide array of MOF topologies that may cater to the specific materials requirements in catalysis, drug delivery, or gas separation.[2] Often, the same node and linker can form from different reagents (e.g., metal salts) and into a variety of products with differing connectivities, topologies, and even compositions.[3] As a consequence, typical MOF syntheses can yield two or more phases, sometimes even in the same reaction mixture.[3b] In some cases, mixtures of phases can occur in the same particle, or even within the same crystallite, as intergrowths or nanoscale inhomogeneities, illustrating the complexity of framework crystallization processes and structuring.[3b] Such phenomena are particularly prevalent in Zr-based MOFs. Pyrene-based NU-1000, for example, can contain structural motifs of the polymorph NU-901 in the center of the crystal.[4] Even though both NU-1000 and NU-901 consist of eight-connected Zr-clusters, NU-901 has tetragonal pores with lower pore volume compared to the hexagonal pores in NU-1000.[4] On the other hand, UiO-66 was shown to often contain domains of the ordered missing cluster phase reo UiO-66, in which one quarter of the Zr-oxo clusters is absent.[5] In both cases, these characteristics have a decisive impact on pore sizes and consequently the material properties.[3a] The situation is further complicated by the fact that many synthetic protocols additionally require the formation of the inorganic nodes themselves from precursor species, prior to framework formation. For example, hexanuclear Zr-oxo nodes are expected to form from the $ZrCl_4$ or $ZrOCl_2 \cdot 8H_2O$ precursors in the synthesis of Zr-based MOFs built from $Zr_6O_4(OH)_4$ clusters.[6] Recent studies have begun to more specifically delineate the effects of synthetic parameters like pH, precursor source and concentration, and solvent type on the cluster structures formed in solution.[7]

In general, a wide variety of parameters affect the cluster formation, nucleation, and growth of MOF crystals, including

C. Koschnick, M. W. Terban, S. Canossa, R. E. Dinnebier, B. V. Lotsch
Nanochemistry Department
Max Planck Institute for Solid State Research
Heisenbergstraße 1, 70569 Stuttgart, Germany
E-mail: b.lotsch@fkf.mpg.de

C. Koschnick, B. V. Lotsch
Department of Chemistry
University of Munich
Butenandtstraße 5–13, 81377 Munich, Germany

C. Koschnick, B. V. Lotsch
Center for Nanoscience
Schellingstraße 4, 80799 Munich, Germany

M. Etter
German Electron Synchrotron (DESY)
Notkestraße 85, D-22607 Hamburg, Germany

The ORCID identification number(s) for the author(s) of this article can be found under https://doi.org/10.1002/adma.202210613.

**ADVANCED
SCIENCE NEWS**

www.advancedsciencenews.com

**ADVANCED
MATERIALS**

www.advmat.de

temperature, pressure, pH, solvent, precursors, or choice of modulators to compete with the linker and allow for more controlled MOF growth.[8] During the synthesis of NU-1000, for example, using biphenyl-carboxylic acid instead of benzoic acid as the modulator prevents the formation of the denser NU-901 phase, allowing for the synthesis of phase pure NU-1000 particles.[9] Importantly, water is known to play a crucial role during the formation of Zr-based MOFs.[8e] In fact, the formation of $Zr_6O_4(OH)_4$ clusters requires hydrolysis of the $ZrCl_4$ or $ZrOCl_2 \cdot 8H_2O$ precursors.[3a,8e,10] The amount of water added during synthesis of Zr-based MOFs can therefore influence both the phase of the formed MOFs, the crystallization rate, and the resulting particle size.[8e,10c,11] When synthesizing UiO-66, for example, a higher water content in the reaction increases the formation rate of the $Zr_6O_4(OH)_4$ clusters, which in turn enhances the rate of crystallization of UiO-66.[11] On the contrary, when no water is present, $Zr_6O_4(OH)_4$ clusters do not form and instead, reaction at 220 °C yields the polymorph MIL-140A which consists of Zr_2O_2 chains.[3a] However, investigation into the role of water on the formation of Zr-MOFs and potential intermediates remains sparse to date.

The many factors that influence the growth of MOF particles allow a great deal of control and tuning of the reaction conditions toward the formation of a desired product. At the same time, however, the multitude of factors and their complex interplay inherently leads to a high level of irreproducibility in the synthesis of phase-pure MOFs, especially when the crystallization pathway of a MOF is unknown. This is especially apparent in porphyrinic Zr-based MOF formation, where the phase formed depends on the modulator used, its concentration, the reaction temperature and time, and other less controllable factors.[8c,12] Synthesis of these MOFs thus often involves laborious screening of reaction conditions between research groups, leading to the existence of multiple synthetic protocols for the same MOF, but also formation of different phases when seemingly following the same protocol. This greatly impedes scientific progress in MOF chemistry and results in rejection for the use of these materials in large scale applications.[12b,13]

Understanding the critical instances during MOF formation can help to better control the growth of phase-pure products as well as help to decipher the complex landscape of MOF formation and potentially address formation of previously unknown MOF phases. Despite vast research efforts, the nucleation and growth processes of MOFs remain a black box for most frameworks. One reason is that the crystallization path not only depends on the composition of the reaction mixture, but also on sometimes subtle changes in reaction conditions.[8a,14] Two common models exist to describe the formation of MOFs: classical and non-classical. In the classical pathway, the monomers (i.e., linker and metal nodes) first spontaneously form crystalline nuclei, which then grow into well-faceted MOF crystals via the sequential layer-by layer deposition of building units onto the nuclei.[15] An example of this is HKUST-1, where the MOF particles were shown to grow directly from solution.[16] The non-classical pathway comprises multiple steps during which clusters of metal ions and linkers aggregate to form non-crystalline intermediates, which then transform into crystalline MOFs.[17] ZIF-8, for example, nucleates from solution via three distinct steps. Initially, the solution separates into solute-rich and solute-poor regions. Subsequently, the solute-rich phases condense into dense amorphous metal–organic aggregates, which in turn crystallize to MOF nanoparticles in the third step.[17] Synthesis of MOF-5 in turn was shown to form crystalline $Zn_5(OH)_8(NO_3)_2 \cdot 2H_2O$–1,4-BDC (BDC = 1,4-benzenedicarboxylate) nanoplatelets at first. These aggregate into layered inorganic–organic composites followed by nucleation of MOF-5 inside the composite.[14c] Given the variability and complexity of these formation processes, it is necessary to study formation mechanisms and synthetic protocols for individual systems in order to understand and, hopefully, gain better control over the formation of phase-pure products.

This work sheds light on the formation mechanism of disordered PCN-224 (dPCN-224), a porphyrin-based Zr-MOF belonging to one of the most prominent classes of frameworks (**Figure 1**a). Different structures were originally published as PCN-221 and MOF-525, but the presence of disordered Zr_6 clusters and a large percentage of linker vacancies was recently identified, helping to establish it as a disordered variation of PCN-224.[18] As laid out in our previous publication, the synthesis of phase-pure dPCN-224 is challenging and often yields multiphase mixtures of porphyrinic MOFs instead.[8c,12b] Besides dPCN-224, six more MOF structures were reported from the same building blocks (Figure 1b–g) with coordination numbers of the Zr-oxo clusters varying from 6 to 12: PCN-224 (6-connected), PCN-222/MOF-545, PCN-225, and NU-902 (all 8-connected), and PCN-223 and MOF-525 (both 12-connected).[13a,19] The different frameworks can have different lattices (e.g., dPCN-224 and PCN-222 are cubic and hexagonal, respectively) as well as variable ordering of linker vacancies (dPCN-224 has disordered linker vacancies and cluster orientations compared to PCN-224, see above), both of which affect the resulting properties.[18,19c,d,20] Synthesis of a phase pure product is therefore key when studying structure–property relationships toward improved functionality in, for example, (photo)catalysis or adsorption related applications.

Here, we study the formation of dPCN-224 and the effects of Zr source, thereby reporting a non-classical nucleation pathway via an intermediate state. Our study is arranged as follows: First, we discuss the effects of the Zr source and water content on the MOF product. Then, we discuss the formation pathway of dPCN-224 using different Zr sources, step-by-step, as investigated using powder X-ray diffraction (PXRD), pair distribution function (PDF) analysis, and scanning electron microscopy (SEM). Finally, we conclude by discussing the important role of water during the synthesis of phase pure dPCN-224, and more generally Zr-based MOFs.

2. Results and Discussion

2.1. Role of the Zirconium(IV) Chloride Source and Water Content on Product Formation

Our investigations were set into motion by a timely discovery; we observed the formation of different products depending on the storage conditions of the precursor material. Two different $ZrCl_4$ sources were used: $ZrCl_4$ that had remained stored in a glovebox ($ZrCl_4$_GB) and $ZrCl_4$ that had been
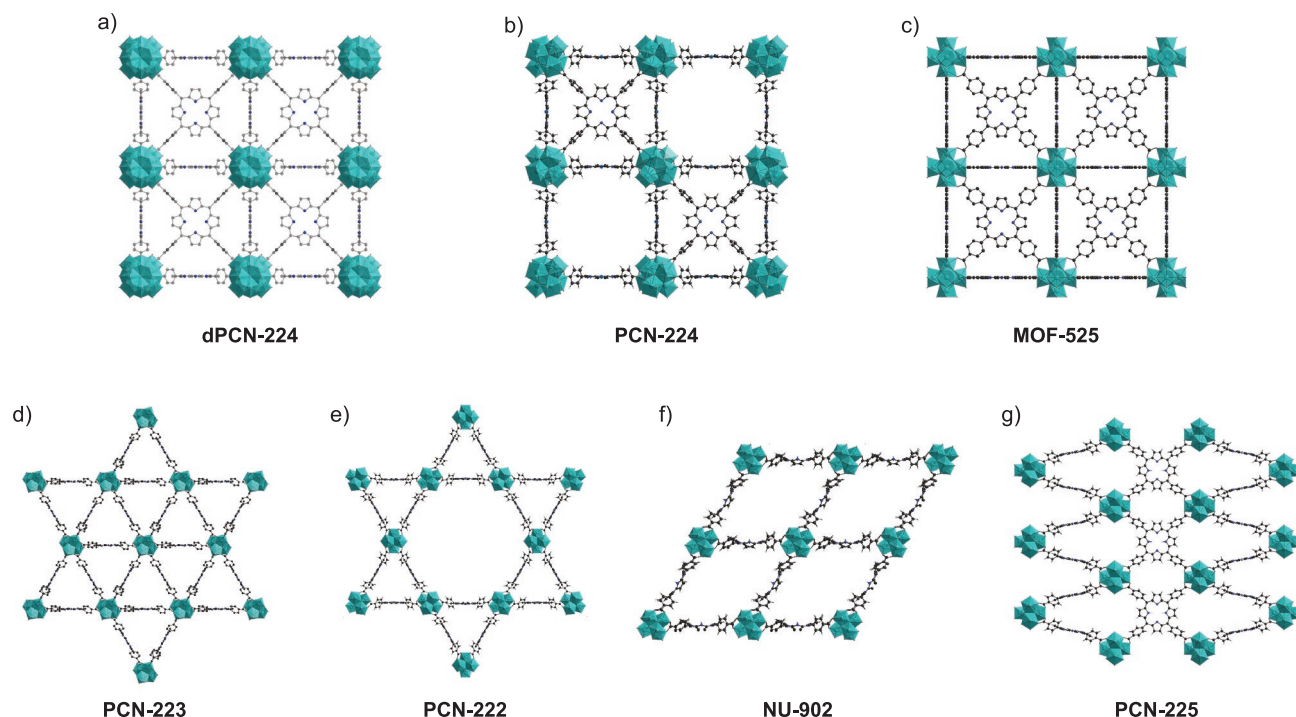
Figure 1. Structures of a) dPCN-224 with disordered linker vacancies,[18] b) PCN-224,[19a] c) the as-reported MOF-525 model,[13a] d) PCN-223,[19b] e) PCN-222,[19d] f) NU-902,[19c] and g) PCN-225.[19e] All MOFs are built from $Zr_6O_4(OH)_4$ clusters and tetrakis (4-carboxyphenyl)porphyrin (TCPP) linkers.

stored in a closed jar under ambient conditions for several months prior to synthesis (ZrCl₄_lab) (see Figures S1–S6, Supporting Information, for more information on precursors). A solvothermal reaction was performed according to a procedure published for PCN-224 by reacting $ZrCl_4$ and tetrakis(4-carboxyphenyl)porphyrin (TCPP) linker under addition of benzoic acid as modulator.[19a] ZrCl₄_GB and ZrCl₄_lab yielded different products after a 24 h reaction. Neither yielded PCN-224 (i.e., the structure with ordered linker vacancies, indicated by superstructure reflections at 3.2° and 5.5° 2θ as shown by PXRD analysis [**Figure 2**a,b]). Instead, ZrCl₄_lab yielded the dPCN-224 variant dPCN-224, whereas ZrCl₄_GB resulted in an unknown, disordered product. Notably, only a few sharp reflections are observed in the PXRD pattern for the unknown product, which occur at similar positions to the (h00) (where h = 2n) reflections of dPCN-224 (Figure 2b).[18] SEM imaging shows cubic particles as expected for dPCN-224 synthesized from ZrCl₄_lab, but highly anisotropic, rod-shaped particles from ZrCl₄_GB (Figure 2c,d).

Nitrogen sorption measurements were used to determine the porosity and surface area of the product materials (Figure 2e,f and Section S4, Supporting Information). ZrCl₄_lab showed a Type I isotherm with micropores of 2.0 nm and a Brunauer–Emmett–Teller surface area of 2288 m² g⁻¹. In contrast, the rod-shaped particles obtained from ZrCl₄_GB showed a Type II isotherm, typical for non-porous or macroporous structures.[21]

Why did ZrCl₄_lab promote the formation of dPCN-224, while ZrCl₄_GB did not? In fact, PXRD analysis revealed that the different $ZrCl_4$ storage conditions result in different precursor materials. While ZrCl₄_GB was found to contain a mixture of the monoclinic[22] and orthorhombic[23] $ZrCl_4$ phases,

ZrCl₄_lab—which had aged in the lab over several months—showed a completely different set of peaks with a significantly lower crystallite size (Figures S3–S5, Supporting Information). As of yet, we could not match the pattern to any known structures.

Further tests were carried out to investigate the effects of storage time and geometry on the precursor. We left ZrCl₄_GB to age under ambient conditions for up to 3 days, making ex situ PXRD measurements. In this instance, we found that the products showed a completely different pattern than for ZrCl₄_lab. The precursors aged for 1 and 3 days (ZrCl₄_1d and ZrCl₄_3d) were tested as precursors for the MOF synthesis. PXRD analysis showed that both yielded crystalline MOFs when compared to ZrCl₄_GB. Synthesis from ZrCl4_1d yielded a product mixture of the porphyrin-based MOFs PCN-222 and NU-902, while ZrCl₄_3d yielded phase pure dPCN-224 (**Figure 3**a and Figure S7, Supporting Information). With respect to morphology, the use of ZrCl₄_1d resulted in rod-shaped particles characteristic of PCN-222 and NU-902, while ZrCl₄_3d produced cubic particles typical of dPCN-224 and resembling the product obtained from ZrCl₄_lab (Figure 3b,c).[18,19c]

Two separate in situ measurements were performed to track the progression of ZrCl₄_GB on exposure to ambient air (at 50%RH in the laboratory). In one test, we spread fresh ZrCl₄_GB across polyimide tape with a high surface area exposed to air and measured PXRD in a transmission geometry. In the second test, the fresh ZrCl₄_GB powder was loaded into a polyimide capillary with one end open and pinholes poked along the sides. During the former test, the starting $ZrCl_4$ phases were observed to rapidly transform, first forming the material observed for ZrCl₄_lab in under 2 min, and then

**ADVANCED
SCIENCE NEWS**

www.advancedsciencenews.com
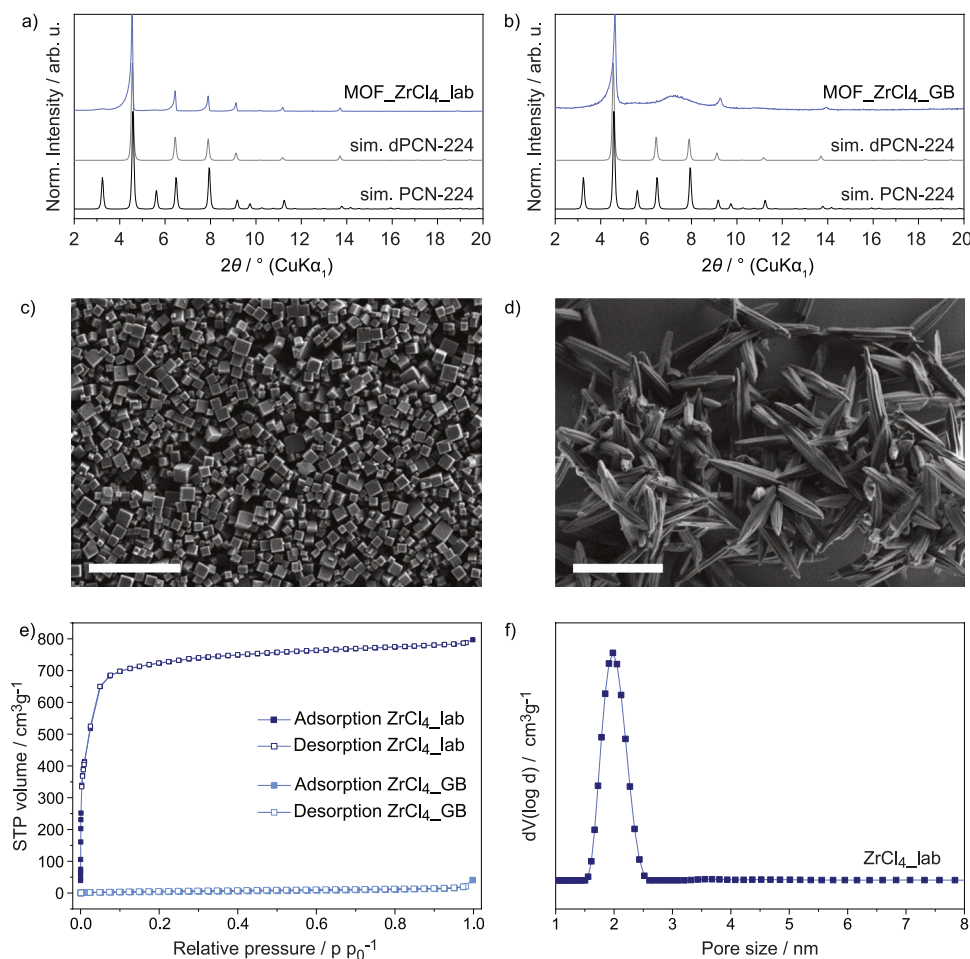
**ADVANCED
MATERIALS**

www.advmat.de

Figure 2. PXRD patterns of products obtained from a) $ZrCl_4$_lab and b) $ZrCl_4$_GB after 24 h reaction time compared to the simulated (sim.) patterns of dPCN-224[18] and PCN-224.[19a] SEM images of products obtained from c) $ZrCl_4$_lab and d) $ZrCl_4$_GB; scale bar = 5 µm. e) Nitrogen sorption isotherm (77 K) of products obtained from $ZrCl_4$_lab and $ZrCl_4$_GB after 24 h reaction time. f) Pore size distribution of the product obtained from $ZrCl_4$_lab.

further transforming to the material observed for $ZrCl_4$_1d and $ZrCl_4$_3d within ≈20 min (Figures S4 and S5, Supporting Information). The observed behavior may be explained by the (partial) hydrolysis of hygroscopic $ZrCl_4$ when exposed to ambient air, forming $ZrOCl_2 \cdot 8H_2O$, correctly expressed as $[Zr_4(OH)_8(H_2O)_{16}]Cl_8 \cdot 12H_2O$ (Figure S5, Supporting Information), suggesting that the amount of water in the reaction mixture is impacted and influences product formation. We attempted to index the phases using structures in the Inorganic Crystal Structure Database as well as reference patterns contained in the Powder Diffraction File of the International Centre for Diffraction Data. The first two peaks of the $ZrCl_4$_3d-type materials do, in fact, show similar positions to the peaks tabulated for the $ZrOCl_2 \cdot 8H_2O$ structures, however there is not an unambiguous indexing, with some similarities to other proposed hydration states (Figure S5, Supporting Information). The phase(s) present in $ZrCl_4$_lab do not show any major similarities to the referenced patterns, though it appears from the in situ measurements that this should be at an earlier stage of hydration/hydrolysis. In the capillary test, we found no major transformation, even after 17 h, (Figure S4, Supporting Information). The results suggest that transformation readily occurs

at the surface, which can then act as a barrier to further water uptake into the bulk. Thus, uncontrolled, a batch of precursor exposed to any air is likely to contain a heterogeneous distribution of states from anhydrous to fully hydrolyzed, depending on, for example, the geometry of the storage container and where the batch is sampled.

To test the role of water in phase formation, apart from the precursor, the reaction was also performed with $ZrCl_4$_GB, after addition of 20–50 µL water (2.2 and 5.5 eq. H_2O compared to $ZrCl_4$) yielding $ZrCl_4$_20µL and $ZrCl_4$_50µL, respectively. When 20 µL of water was added to the reaction, a mixture of PCN-222/NU-902 was formed after 24 h, similar to the synthesis from $ZrCl_4$_1d (Figure 3a and Figure S8, Supporting Information). In contrast, addition of 50 µL water yielded dPCN-224 (Figure S9, Supporting Information). Compared to the synthesis from $ZrCl_4$_GB, the addition of water directly to the reaction therefore also promoted the formation of crystalline frameworks built from $Zr_6O_4(OH)_4$. SEM images show that sample $ZrCl_4$_20µL formed thin rods that aggregated onto the surface of hexagonal rods (Figure 3d), while sample $ZrCl_4$_50µL yielded intergrown, cubic particles (Figure 3e). Overall, these findings suggest that the degree of $ZrCl_4$ hydrolysis, or likewise the
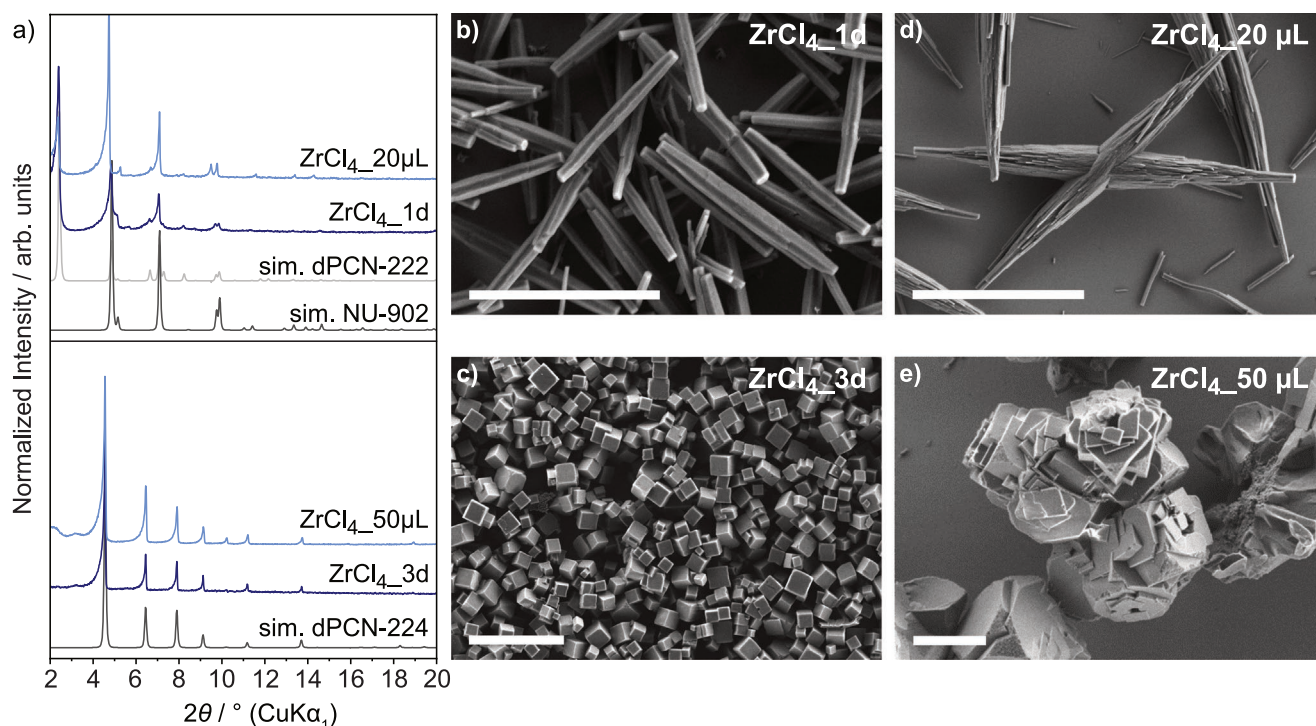
Figure 3. a) PXRD patterns of the products obtained from ZrCl$_4$_GB that was left to age for 1 day (ZrCl$_4$_1d) and 3 days (ZrCl$_4$_3d) prior to reaction, and from ZrCl$_4$_GB under addition of 20 µL (ZrCl$_4$_20µL) and 50 µL (ZrCl$_4$_50µL) water compared to the simulated patterns of dPCN-224, PCN-222, and NU-902. SEM images of the products obtained from b) ZrCl$_4$_1d, c) ZrCl$_4$_3d, d) ZrCl$_4$_GB with 20 µL water, and e) ZrCl$_4$_GB with 50 µL water. Scale bar = 5 µm.

quantity of water in the reaction, guides framework formation and is essential for the growth of dPCN-224.

2.2. Time-Dependent Study from Different Zirconium(IV) Chloride Sources

To further elucidate the crystallization process of dPCN-224, time-dependent experiments were carried out during the synthesis from both ZrCl$_4$_GB and ZrCl$_4$_lab (see Sections S1, S4, and S5, Supporting Information, for further details). PXRD analysis and SEM imaging of the products revealed that multiple products were formed during the reactions (**Figures 4** and **5**).

Synthesis from ZrCl$_4$_GB yielded two different product types, depending on the reaction time (Figure 4). Synthesis times of less than 1 h led to string-like particles with a width of ≈30–50 nm consisting of an unknown first phase. The PXRD pattern could not be assigned to any known Zr-TCPP-based framework. When the reaction time was extended to 24 h, we observed the formation of a second unknown phase with reflections at 4.64°, 9.28°, and 13.93° 2θ. Increase of the reaction time up to 20 days led to an apparent aggregation of the anisotropic particles (SEM), but did not substantially change the phase structure (PXRD), suggesting that dPCN-224 cannot form from ZrCl$_4$_GB.

Similarly, the use of ZrCl$_4$_lab also yielded two unknown products at the beginning of the reaction with PXRD patterns resembling those of the products obtained from ZrCl$_4$_GB

(Figure 5), suggesting a similar initial reaction pathway. However, unlike ZrCl$_4$_GB, further transformation was observed with increasing reaction time. Reaction for 2 h yielded a mixture of hexagonal PCN-222 and cubic dPCN-224. Increasing the reaction time to 6 and 18 h decreased PCN-222 in favor of dPCN-224. After 24 h, phase pure dPCN-224 was obtained.

Corresponding SEM imaging showed changes of the MOF particle morphologies over time. Similar to ZrCl$_4$_GB, string-like particles were obtained after 2 min and 1 h, respectively. Remarkably, few cubic particles grew on the surface of the rods after 1 h. As the reaction time increased, thicker hexagonal rods were observed, which are characteristic of PCN-222.[19c] From 2–18 h, a large number of truncated cubes in the size range of 300–600 nm, and later up to 5 µm, grew from the surface and appeared to consume the rods (Figure 5 and Figure S12, Supporting Information). After 24 h, no rods were left, and the remaining dPCN-224 particles adopted a cubic morphology with sizes between 400 and 700 nm.

2.3. Identifying the Unknown Phases Formed during Synthesis from Zirconium(IV) Chloride

During the reactions of both ZrCl$_4$_lab and ZrCl$_4$_GB, the first product obtained after short reaction times consisted of particles with a string-like morphology. Elemental analysis revealed that this product is purely organic and energy dispersive X-ray analysis showed the presence of chloride in the sample (Sections S6 and S7, Supporting Information).
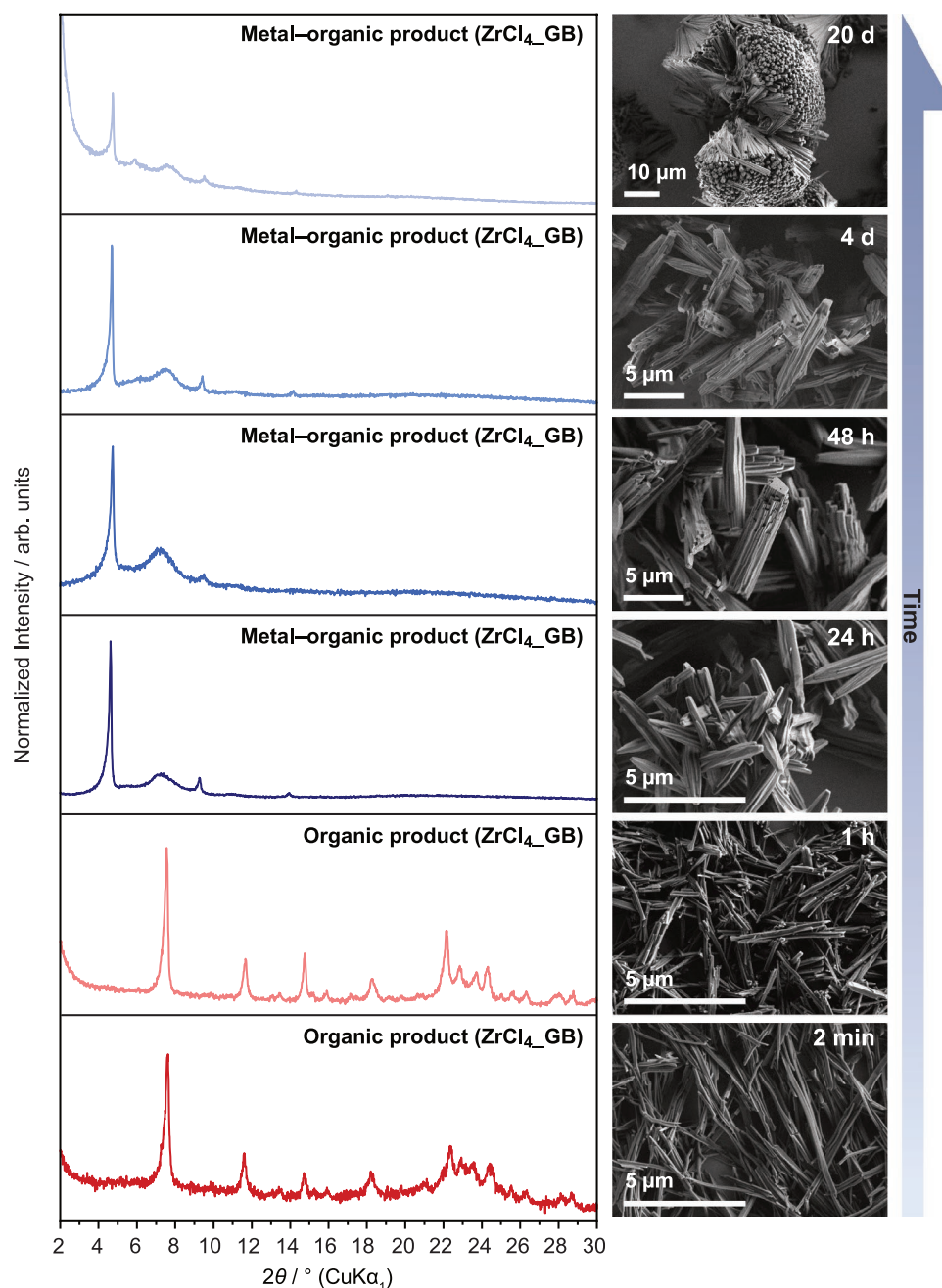
**ADVANCED
SCIENCE NEWS**

www.advancedsciencenews.com

**ADVANCED
MATERIALS**

www.advmat.de

Figure 4. PXRD patterns (left) and SEM images (right) from the products obtained during synthesis from ZrCl$_4$_GB after 2 min, 1, 24, 48 h, 4, and 20 days reaction time. After 2 min and 1 h an organic product was formed whereas reaction for 24, 48 h, 4, and 20 days yielded a metal–organic product.

NMR spectroscopy was used to probe the organic products. The product only consisted of TCPP and did not contain the benzoic acid modulator (Figure S19, Supporting Information). The intense green color (Figure S23, Supporting Information) of the product indicated that the TCPP species was protonated.[24] Neutral TCPP (H$_2$TCPP) can be successively protonated to form the monocationic (H$_3$TCPP$^+$) and dicationic (H$_4$TCPP^{2+}) forms, thereby changing the color from purple to green.[24,25] The combined evidence suggests that for both sources, the initial product consists of molecular H$_4$TCPP^{2+} crystals, where the positive charges are balanced

by chloride anions. The crystal structure of this TCPP phase will be subject of future studies.

After the formation of the H$_4$TCPP^{2+}-based intermediate, a second unknown intermediate formed during the synthesis from both Zr sources. This product was isolated after 1 h when employing ZrCl$_4$_lab, and after 24 h–20 days when employing ZrCl$_4$_GB. NMR analysis after digestion confirmed the presence of both TCPP and benzoic acid (Figures S20–S22, Supporting Information), and elemental analysis revealed that this second product contained Zr (Table S4, Supporting Information). In other words, a metal–organic compound formed at
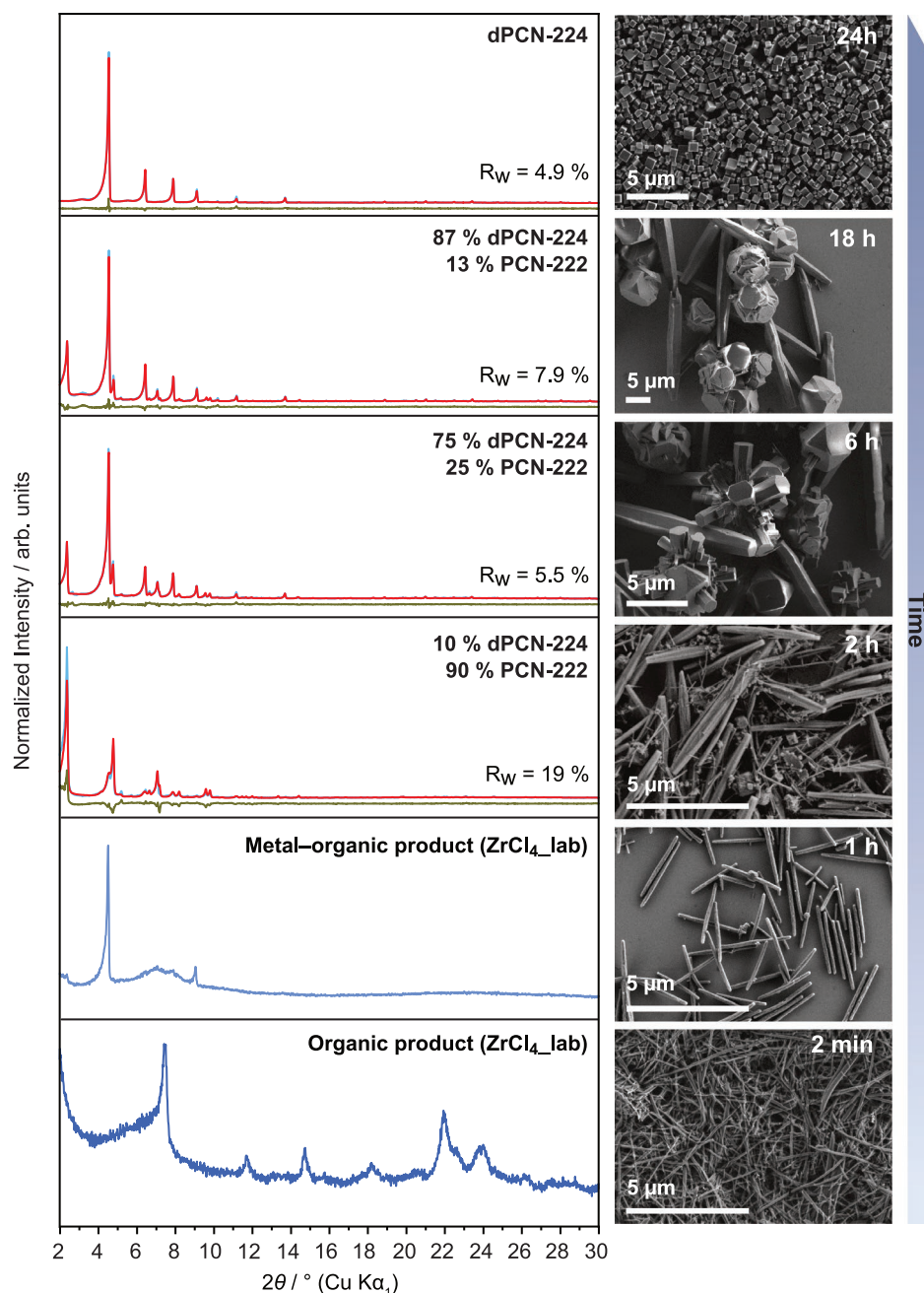
Figure 5. PXRD patterns from the products obtained during synthesis from ZrCl$_4$_lab after 2 min and 1 h reaction time, and Rietveld refinements and residual values Rw of PCN-222[19d] and dPCN-224[18] against observed patterns from the products obtained during synthesis from ZrCl$_4$_lab after 2, 6, 18, and 24 h reaction time (left). After 2 min a first unknown phase (organic product) was formed, whereas reaction for 1 h yielded a second unknown phase (metal–organic product). The SEM images show a transformation of the particles' morphology with increasing reaction time (right).

this stage of the reaction. PXRD analysis showed reflections at similar angles to the 200, 400, and 600 reflections in dPCN-224, indicating a periodic ordering similar to dPCN-224 along at least 1D. Electron diffraction also showed 1D order with a periodicity of ≈19.65 Å, in agreement with the PXRD data and the intercluster spacing of dPCN-224 (Figure S24, Supporting Information).

To understand the local structure, the samples formed from ZrCl$_4$_GB after 24 h and 20 days (ZrCl$_4$_GB_24h and

ZrCl$_4$_GB_20d) and the samples formed from ZrCl$_4$_lab after 1 and 24 h (ZrCl$_4$_lab_1h and ZrCl$_4$_lab_24h) were investigated with PDF analysis (**Table 1**, **Figure 6**, and Section S11, Supporting Information). Interestingly, the local structure from 0 to 10 Å differs significantly between the samples obtained from ZrCl$_4$_GB and ZrCl$_4$_lab. The PDFs of ZrCl$_4$_lab_1h and ZrCl$_4$_lab_24h, which consist of the metal–organic intermediate compound and dPCN-224, respectively, are very similar. Both PDFs feature peaks at 2.24, 3.53, and 4.92 Å. These correspond

**ADVANCED
SCIENCE NEWS**

www.advancedsciencenews.com

**ADVANCED
MATERIALS**

www.advmat.de

Table 1. Comparison of samples characterized via pair distribution function analysis indicating the Zr source, reaction time, and Zr node that best describes the local structure.

Sample	Zr source	Reaction time	Zr nodes
ZrCl$_4$_lab_1h	ZrCl$_4$_lab	1 h	Zr$_6$O$_8$
ZrCl$_4$_lab_24h	ZrCl$_4$_lab	24 h	Zr$_6$O$_8$
ZrCl$_4$_GB_24h	ZrCl$_4$_GB	24 h	Best described by [Zr$_2$O$_2$]$_2$
ZrCl$_4$_GB_20d	ZrCl$_4$_GB	20 days	Best described by Zr$_2$O$_2$ dimers, Zr-oxo chains, or Zr$_4$O$_7$ tetramers

to Zr–O, adjacent Zr–Zr, and diagonal Zr–Zr pair distances in a Zr$_6$O$_8$ cluster.[18] The inorganic nodes in the ZrCl$_4$_lab_1h sample therefore consist of Zr$_6$O$_8$ clusters revealing that the hexanuclear Zr clusters in dPCN-224 form already during the early stages of the reaction.

Differences in cluster formation as a function of water content are expected. Several studies highlight the key role of water content in metal-oxide cluster formation. Ragon et al. showed that in the absence of water, reaction of ZrCl$_4$ and BDC in *N,N*-dimethylformamide (DMF) formed an amorphous product instead of UiO-66.[11] They argued that water is needed to form the secondary building unit Zr$_6$(μ_3–O)$_4$(μ_3–OH)$_4$(CO$_2$)$_{12}$, and hence UiO-66.[11] Another study by Butova et al. showed that in the absence of water, the MOF polymorph MIL-140A built of Zr$_2$O$_2$ chains forms instead of UiO-66.[3a] Leubner et al. further reported that MIL-140A forms from dense, layered Zr$_2$O$_2$(OAc)$_2$(BDC) (OAc = acetate) intermediates that further transform into porous MIL-140.[26] This last example may suggest an analogous pathway for the dPCN-224 formation observed from ZrCl$_4$_GB where an intermediate formed before

nucleation of dPCN-224 particles. Recently, a study of structures forming in solution found that [Zr$_4$(OH)$_8$(OH$_2$)$_{16}$]$^{8+}$-tetramers, the same found in the crystal structure of ZrOCl$_2$·8H$_2$O, are preferred in aqueous solution.[7b]

Inspired by this, we compared the experimental PDFs of ZrCl$_4$_GB_24h and ZrCl$_4$_GB_20d—which did not form Zr$_6$O$_4$(OH)$_4$ clusters—to simulated PDFs of a variety of Zr-oxo species including [Zr$_2$O$_2$]$_x$ chains of different lengths ($x = 2, 3,$ or, 6), derived from a Zr$_2$O$_2$(OAc)$_2$(BDC) precursor (Section S11, Supporting Information).[26] Interestingly, the [Zr$_2$O$_2$]$_x$ chain models include the peak at 3.95 Å, which corresponds to next-nearest neighbor Zr–Zr distances between two Zr$_2$O$_2$ units (**Figure 7**a,b).

When comparing the PDF of ZrCl$_4$_GB_20d to the simulated PDFs Zr$_6$O$_8$ clusters versus [Zr$_2$O$_2$]$_2$, the Pearson correlation coefficient (PCC), which measures the linear correlation between experimental and theoretical PDFs, increased from 0.587 to 0.837. Thus, the inorganic nodes in ZrCl$_4$_GB_20d show higher similarity to short segments of [Zr$_2$O$_2$]$_x$ chains.

The experimental PDF of ZrCl$_4$_GB_24h agrees less well with the simulated PDF of the [Zr$_2$O$_2$]$_2$ model (PCC = 0.723) (Figure 7a). In fact, when comparing the PDF of ZrCl$_4$_GB_24h to the PDF of ZrCl$_4$_GB_20d, the next-nearest neighbor Zr–Zr distance increases from 3.38 to 3.45 Å and the intensity of the peak at 3.95 Å decreases, which may indicate either a different arrangement of Zr atoms in the inorganic nodes or a different distribution of cluster types. For instance, the PDF of ZrCl$_4$_GB_24h showed the best agreements for Zr$_2$O$_2$ dimers, Zr-oxo chains, or Zr$_4$O$_7$ tetramers (Figure 7c–e).

As discussed above, synthesis from both ZrCl$_4$_lab and ZrCl$_4$_GB yielded metal–organic compounds with a periodicity of 19 Å, which suggests alternating Zr nodes and TCPP linkers.
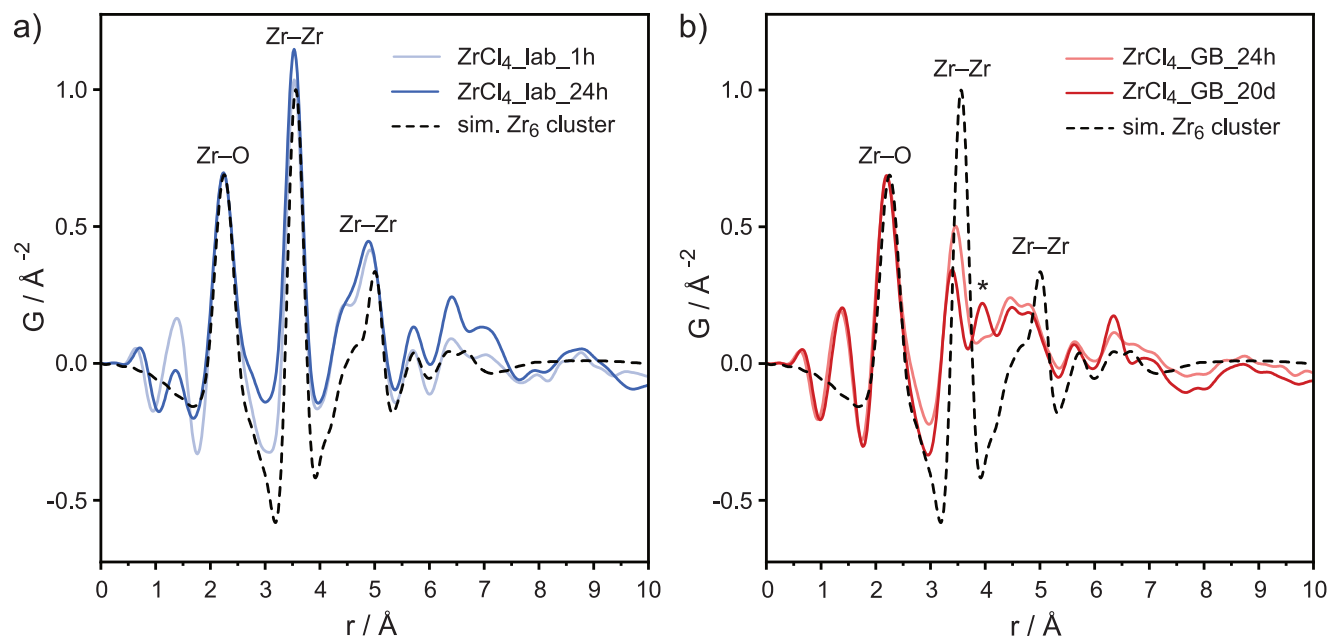

Figure 6. a) Experimental PDFs of ZrCl$_4$_lab_1h and ZrCl$_4$_lab_24h after 1 and 24 h reaction, respectively, compared to the simulated (sim.) PDFs of a Zr$_6$O$_8$ cluster. b) Experimental PDFs of ZrCl$_4$_GB_24h and ZrCl$_4$_GB_20d after 24 h and 20 days reaction, respectively, compared to the simulated PDFs of a Zr$_6$O$_8$ cluster. Compared to ZrCl$_4$_GB_24h, the PDF of ZrCl$_4$_GB_20d features a peak at 3.95 Å (*) which likely corresponds to next-nearest neighbor Zr–Zr distances between two Zr$_2$O$_2$ units. The first peak in the experimental PDFs at ≈1.4 Å comes from nearest neighbor pairs within the TCPP linkers.
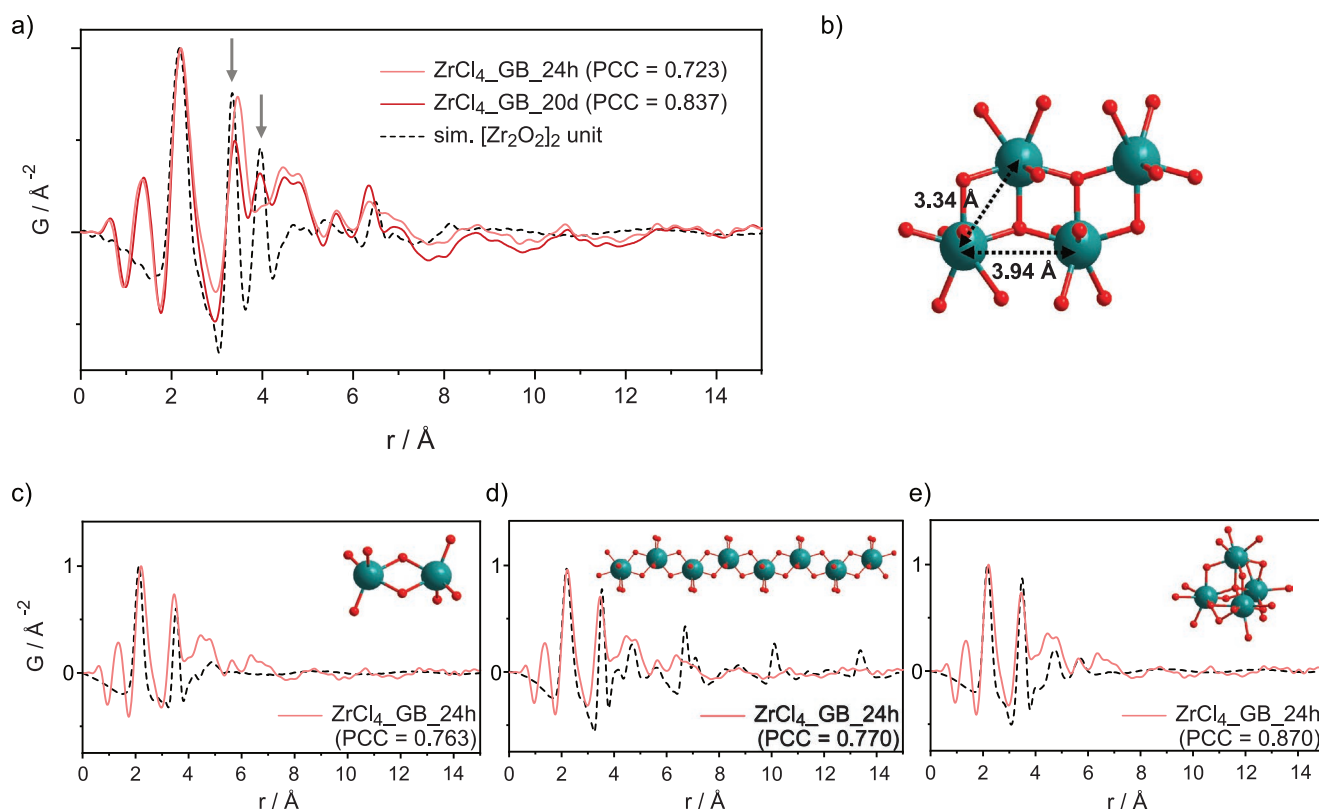
Figure 7. a) Experimental PDFs of ZrCl$_4$_GB_24h and ZrCl$_4$_GB_20d compared to the simulated (sim.) PDF of a [Zr$_2$O$_2$]$_2$ unit. b) [Zr$_2$O$_2$]$_2$ unit with nearest and next-nearest Zr–Zr distances of 3.34 and 3.94 Å, respectively. c–e) Experimental PDFs of ZrCl$_4$_GB_24h compared to sim. PDFs of a Zr$_2$O$_2$ dimer, a [ZrO$_2$]$_3$ chain, and a Zr$_4$O$_7$ tetramer, respectively, which are shown in insets. The PCC value corresponds to Pearson correlation coefficient. All PDF curves have been renormalized for visual comparison such that the height of the Zr-O peak equals 1.

Although, since we appear to observe different node structures in the products of ZrCl$_4$_GB, it suggests that similar motifs can form with different Zr-oxo nodes. PDF analysis provided further information on the ordering of products (**Figure 8**). The intermediate-range atomic density distributions from 10–50 Å revealed periodic oscillations for all four samples. The PDF of ZrCl$_4$_lab_24h showed broad features at long distances due to the periodic arrangement of tilted Zr$_6$O$_4$(OH)$_4$ clusters in dPCN-224 and some sharp peaks (e.g., 24–30 Å) due to preferred intercluster Zr–Zr pair distances. As suggested by the few Bragg reflections in reciprocal space, ZrCl$_4$_lab_1h also showed broad, high-r features, albeit at relatively lower intensity compared to those of ZrCl$_4$_lab_24h. It also showed sharp peaks at the intercluster distances (15–30 Å), suggesting that metal–organic oligomers with intermediate-range order between the nearest and next-nearest neighboring Zr$_6$O$_4$(OH)$_4$ clusters formed after 1 h.

The products obtained from ZrCl$_4$_GB at 24 h and 20 days also both showed broad, high-r peaks, but without sharp peaks at the intercluster distances, indicating a different, and possibly more disordered arrangement of Zr nodes along the ordered directions.

The 50–100 Å range gave further insights into the mid-range order (Figure 8). In the PDFs of ZrCl$_4$_lab_1h and ZrCl$_4$_GB_24, the oscillations above 50 Å were weak, indicating a lower distance of coherent ordering, whereas the dPCN-224 sample (ZrCl$_4$_lab_24h) retained oscillation and sharp peaks due to
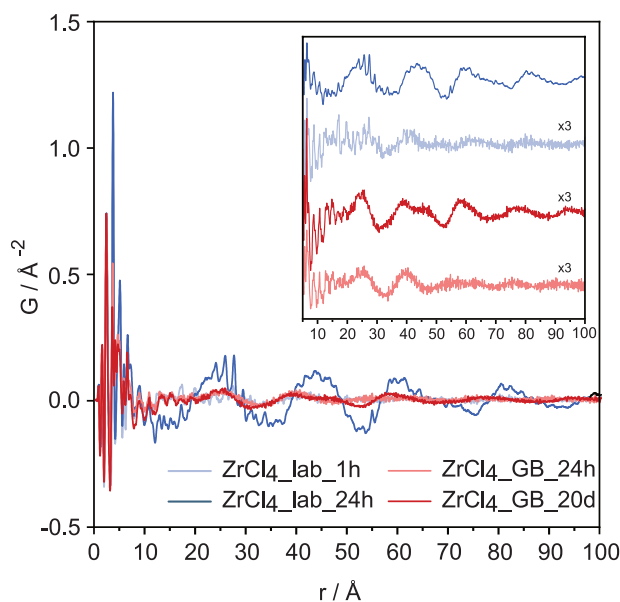

Figure 8. Experimental PDFs of ZrCl$_4$_lab_1h, ZrCl$_4$_lab_24h, ZrCl$_4$_GB_24h, and ZrCl$_4$_GB_20d PDF in the long range. Inset shows enlarged views (scaled ×3) of the oscillation in the long range.

**ADVANCED
SCIENCE NEWS**

www.advancedsciencenews.com

**ADVANCED
MATERIALS**

www.advmat.de

a higher degree of long-range order. ZrCl$_4$_GB_20d featured stronger oscillation in the high-r atomic density distribution relative to the product obtained after a 24 h reaction. Increasing the reaction time therefore yielded a product with longer-range order. Whereas the diffraction peaks for both intermediate and final samples are sharp in reciprocal space, the difference in perceived ordering may partly reflect that the order is 3D in ZrCl$_4$_lab_24h but primarily 1D in the intermediate phases.

To summarize, the use of ZrCl$_4$_lab led to fast formation of Zr$_6$O$_8$ clusters, whereas reaction from ZrCl$_4$_GB produced different clusters, even at extended reaction times. The Zr-oxo nodes formed after 24 h reaction with ZrCl4_GB could not be unambiguously identified, but showed highest similarity to PDFs simulated for Zr$_2$O$_2$ dimers, ZrO chains, or Zr$_4$O$_7$ tetramers, whereas the product formed after 20 days appears to favor [Zr$_2$O$_2$]$_2$-like units. All compounds featured periodic arrangement of altering Zr nodes and TCPP molecules in the intermediate range, and the ordering increased with increasing reaction times.

2.4. Control Experiment Using Zirconyl Chloride as a Zirconium Source

To further test the effects of precursor type and water content, we used ZrOCl$_2$·8H$_2$O as the Zr source, which is also widely used for the synthesis of porphyrin-based Zr-based MOFs, and conducted the same time-dependent study. The same one-step procedure was performed as before in which ZrOCl$_2$·8H$_2$O, TCPP, and benzoic acid were reacted in DMF at 120 °C for 15, 30, 60, 90 min, 4, and 24 h (see Table S3, Supporting Information, for further details).

The PXRD patterns revealed a similar formation pathway of dPCN-224 as for ZrCl$_4$_lab. The patterns collected after 15 min to 24 h of reaction time showed a transformation from the 1D ordered, metal–organic intermediate to crystalline dPCN-224 (**Figure 9**). After 30 min, new broad peaks appeared between 3.50° and 10.60° 2θ, suggesting an onset of 3D ordering of the metal–organic intermediate. The PXRD pattern of the product isolated after 1 h showed that dPCN-224 started to form from the intermediate. Longer reaction times yielded dPCN-224 as product. Interestingly, only minor PCN-222 or NU-902 impurities were formed when using ZrOCl$_2$·8H$_2$O (Figure 9 and Figure S10, Supporting Information), unlike the synthesis from ZrCl$_4$.

The morphology of the particles was verified by SEM (Figure 9). Rice-shaped particles of ≈250 nm were formed after 15 min, which transformed into 3–5 µm long rods after 30 min. After 1 h, cubic nanoparticles formed on the surface of the rods, which likely marks the onset of 3D MOF formation. As the reaction progressed, the small cubes grew into 3–4 µm wide intergrown particles and the rods disappeared (Figure S12, Supporting Information). After 24 h, only cubic nanoparticles (200–500 nm) were observed.

PDF analysis revealed that the intermediate formed after 30 min during synthesis with ZrOCl$_2$·8H$_2$O resembles the intermediate formed from ZrCl$_4$_lab after 1 h (**Figure 10**a). Again, the product features the characteristic peaks at 2.24, 3.53, and 4.92 Å, which correspond to the Zr–O, adjacent Zr–Zr, and diagonal Zr–Zr distances of a Zr$_6$O$_8$ cluster. Similar to ZrCl$_4$_lab_1h, the product shows periodic oscillation between 20 and 100 Å, indicating a periodic arrangement of alternating Zr$_6$O$_8$ cluster and TCPP linkers. Compared to ZrCl$_4$_lab_1h, the peaks around 25 and 45 Å are sharper and the oscillation remains strong above 50 Å, which indicates a more ordered structure (Figure 10b). This is in agreement with the PXRD analysis, which showed additional peaks and more ordering in the intermediate formed from ZrOCl$_2$·8H2O (Figure 10c).

2.5. Proposed Mechanism of dPCN-224 Growth

From this study, it is clear that the Zr source and water content influence product formation. While synthesis from neat ZrCl$_4$_GB did not form Zr$_6$O$_8$ clusters and, hence, dPCN-224, synthesis from ZrCl$_4$_lab that had aged under ambient conditions for several months yielded crystalline dPCN-224. Use of ZrOCl$_2$·8H$_2$O as the Zr source, which is also widely used for the synthesis of porphyrin-based Zr-based MOFs, also yielded dPCN-224. In both cases, however, dPCN-224 does not follow the classical nucleation path, that is, it does not homogeneously crystallize from solution (**Figure 11**). Instead, partly disordered intermediates are first formed, consisting of 1D-ordered motifs of alternating linker and node, which are present as highly anisotropic, aggregated rods. Then, nucleation of cubic MOF structures takes place heterogeneously on the surface of the intermediate particles and eventually consumes them, resulting in the final dPCN-224 product.

The observed steps in the synthesis of dPCN-224 from ZrCl$_4$_lab and ZrOCl$_2$·8H$_2$O allow us to propose the following nucleation and growth mechanism for the formation of dPCN-224 under the tested reaction conditions (**Figure 12**). Initially, a purely organic TCPP-based product forms (step 1). It is not clear whether this organic product takes part in the nucleation of metal–organic species or whether it is simply a transient side product. Following this, metal–organic intermediates consisting of Zr$_6$O$_8$ cluster and TCPP molecules form (step 2), which grow into microrods (step 3). The crystallites show 1D periodicity with a repeating unit of 19 Å, suggesting that motifs with an alternating arrangement of Zr$_6$O$_8$ clusters and TCPP molecules are ordered within the rods (Figure S30, Supporting Information). As shown from PDF analysis, the rods feature ordering in the intermediate range between the nearest and next-nearest neighboring Zr$_6$O$_8$ clusters. We speculate that the rod-shaped intermediates consist of a large number of small Zr$_6$O$_8$–TCPP chain-like domains, which are bridged by TCPP molecules. Once the metal–organic rod intermediate is formed, dPCN-224 starts nucleating on the surface of the rods, suggesting that the metal–organic intermediate possibly acts as template and source of Zr-oxo clusters and TCPP linkers (step 4). With increasing reaction times, the dPCN-224 cubes increase in size whilst the intermediate is consumed (step 5). Once the intermediates have been completely consumed, the dPCN-224 crystals progress to a more monodisperse distribution of smaller dPCN-224 single crystals (step 6) in a size-focusing step. Step 6 shares similarities to digestive ripening (or reversed Ostwald ripening) via surface etching of capping agents where smaller particles form at the expense of larger
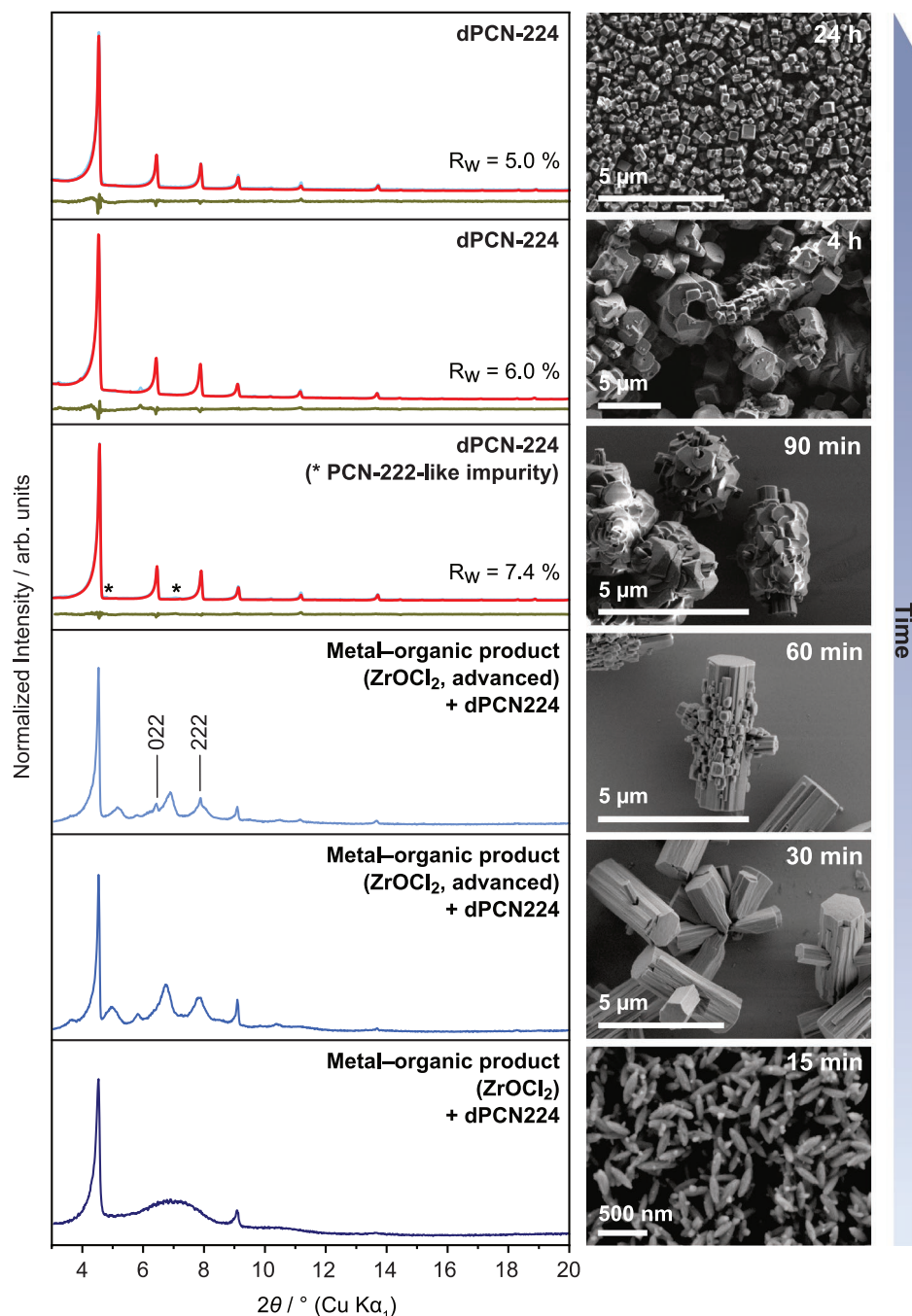
**ADVANCED
SCIENCE NEWS**

www.advancedsciencenews.com

**ADVANCED
MATERIALS**

www.advmat.de

Figure 9. PXRD patterns from the products obtained during synthesis from $ZrOCl_2 \cdot 8H_2O$ after 15, 30, and 60 min reaction time. Rietveld refinements and residual value Rw of dPCN-224 are shown against observed patterns from the products obtained during synthesis from $ZrOCl_2 \cdot 8H_2O$ after 90 min, 4, and 24 h reaction time (left). After 60 min, dPCN-224 started to form as indicated by the peaks at 6.4° and 7.9° 2θ which correspond to the 022 and 222 indices of the dPCN-224 phase. After 90 min, the product mostly consists of dPCN-224 but contains small impurities of a PCN-222-like product, highlighted with an asterisk (*) that could not be modeled (Figure S10, Supporting Information). The SEM images show a transformation of the particles morphology with increasing reaction time (right). Further SEM images are shown in Figure S12, Supporting Information.

particles, and further investigation of this process will be the focus of future work.[27]

It is worth highlighting that PCN-222 forms as intermediates during synthesis of dPCN-224. This is in contrast to other studies on the synthesis of porphyrinic Zr MOFs in which hexagonal PCN-222 was the thermodynamic product compared

to cubic porphyrinic MOFs.[8c,12] Judging from the SEM images during synthesis from $ZrCl_4$, it appears that PCN-222 forms from the same metal–organic intermediate, suggesting a similar formation path for these two MOF phases under the tested conditions before at some point their speciation diverges. Compared to the synthesis from hydrolyzed $ZrCl_4$, only minor
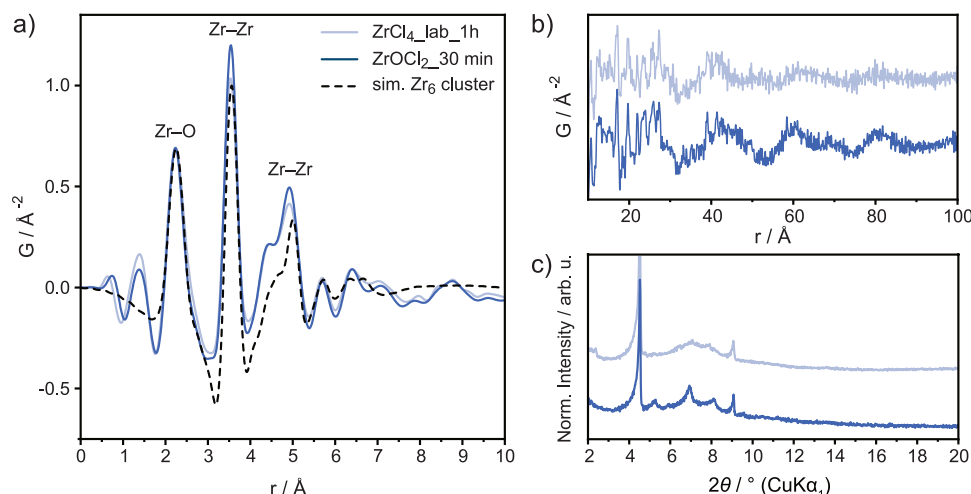
2210613 (11 of 16)

ADVANCED
SCIENCE NEWS

www.advancedsciencenews.com

ADVANCED
MATERIALS

www.advmat.de

Figure 10. a) Experimental PDFs of products obtained from $ZrOCl_2 \cdot 8H_2O$ after 30 min reaction ($ZrOCl_2\_30min$), compared to the PDF of $ZrCl_4\_lab\_1h$ and to the simulated PDF (sim.) of a Zr_6O_8 cluster. b) Experimental PDFs of $ZrOCl_2\_30min$ and $ZrCl_4\_lab\_1h$ showing oscillation in the long range. c) Comparison of the PXRD patterns of $ZrOCl_2\_30min$ and $ZrCl_4\_lab\_1h$.

impurities of a PCN-222-like intermediate are observed when $ZrOCl_2 \cdot 8H_2O$ acts as the Zr source. This could be explained by higher amounts of water in the reaction from the coordinated water in $ZrOCl_2 \cdot 8H_2O$ through which the PCN-222 intermediate vanishes and dPCN-224 forms more quickly.

2.6. Importance of Water on the dPCN-224 Formation

The addition of water to the synthesis of Zr-based MOFs is known to accelerate the formation of the framework. For example, during synthesis of UiO-66, the presence of water increases the formation rate of the $Zr_6O_4(OH)_4$ cluster which in turn allows for faster synthesis of the framework.[11] A similar trend was observed for the formation of dPCN-224 when increasing the amount of water in the reaction (**Figure 13**).

PXRD analysis revealed that reaction from $ZrCl_4\_GB$ with 20 µL water yielded mixtures of PCN-222 and NU-902 between 24 h and 4 days. After 12 days, however, a mixture of cubic dPCN-224 and hexagonal PCN-222 was obtained showing that at longer reaction times dPCN-224 eventually forms. In contrast, synthesis with 50 µL water in the reaction proceeded at a faster rate. After 6 h, the product mostly consisted of dPCN-224 with minor PCN-222/NU-902 like impurities and after 24 h and 4 days reaction time, phase-pure dPCN-224 was obtained. The increase of water in the reaction therefore considerably accelerated the growth of dPCN-224 and reduces the amount of the PCN-222-like intermediate formed during the reaction.
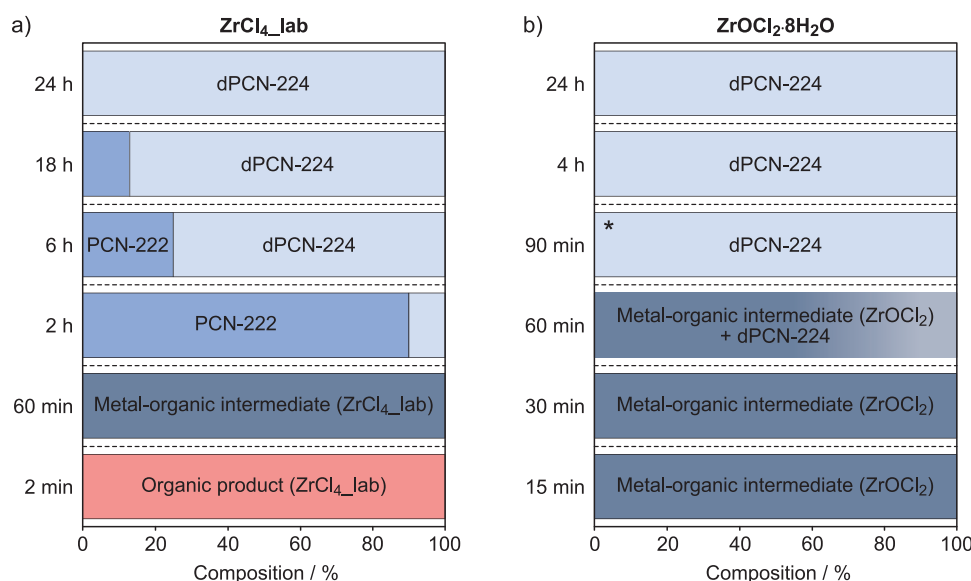

Figure 11. Phase compositions of products isolated after different reaction times during synthesis of dPCN-224 from a) $ZrCl_4\_lab$ and b) $ZrOCl_2 \cdot 8H_2O$. *Synthesis from $ZrOCl_2 \cdot 8H_2O$ after 90 min reaction contained PCN-222/NU-902-like impurities.
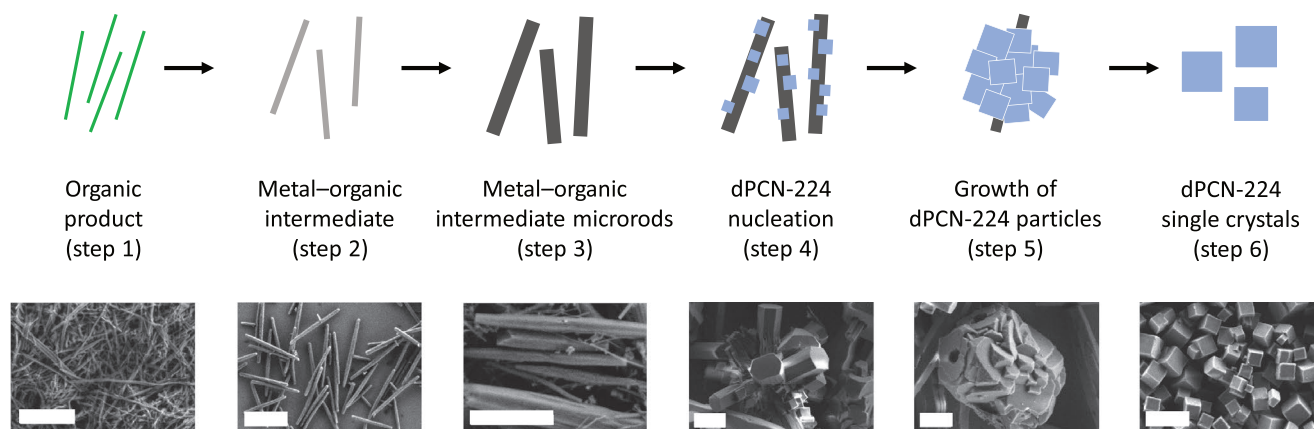
Figure 12. Schematic illustration of the six steps observed during dPCN-224 formation and corresponding SEM images during synthesis from ZrCl$_4$_lab (scale bar = 2 µm).

These findings exemplify the importance of water in the synthesis of dPCN-224, both as a stoichiometric reaction partner and in terms of kinetics. ZrCl$_4$ is hygroscopic and readily hydrolyses to ZrOCl$_2$·8H$_2$O (correctly expressed as [Zr$_4$(OH)$_8$(H$_2$O)$_{16}$]Cl$_8$·12H$_2$O). The aging time of ZrCl$_4$ in ambient conditions thus greatly affected the product formation in a 24 h reaction. In our study, neat ZrCl$_4$ that was left to stand for 1 day (ZrCl$_4$_1d) yielded a mixture of PCN-222 and NU-902 as the products, whereas when left to age for 3 days (ZrCl4_3d), it yielded phase-pure dPCN-224. However, the daily temperature and fluctuations in relative humidity impact the hydrolysis rate of ZrCl$_4$. For instance, in some cases ZrCl$_4$_3d yielded mixtures of dPCN-224 and hexagonal PCN-222 instead of dPCN-24 after 24 h, suggesting that the formation of dPCN-224 was slower, presumably due to less water in the reaction (Figure S11a, Supporting Information). Another point to consider is that DMF is also hygroscopic and will also have varying quantities of water contamination (Table S1, Supporting Information). Reaction from ZrCl$_4$_GB in DMF from a freshly opened bottle and from the same bottle after keeping it in the laboratory for a month yielded different products which further exemplifies the importance of meticulously controlling the water content during synthesis (Figure S11b, Supporting Information). As a matter of fact, the formation of Zr$_6$O$_4$(OH)$_4$ clusters, and thus of dPCN-224 requires hydrolysis of the Zr precursor. Hence, the hygroscopic nature of both ZrCl$_4$ and DMF affects the growth of dPCN-224 and is a primary source for reproducibility issues across reactions and laboratories. The choice of reactants and solvent, but also the relative humidity and temperature all determine the amount of water in the reaction and therefore need to be monitored with caution when synthesizing porphyrinic Zr-based MOFs. More generally, water is expected to have a pronounced influence on the speciation and growth kinetics of all MOFs obtained from an oxophilic zirconium source. While many of these factors are difficult to control, the use of ZrOCl$_2$·8H$_2$O—which already contains coordinated water and is therefore less sensitive to atmospheric moisture—replacing ZrCl$_4$ can reduce the irreproducibility often encountered during synthesis of porphyrinic Zr-based MOFs.[11,28]
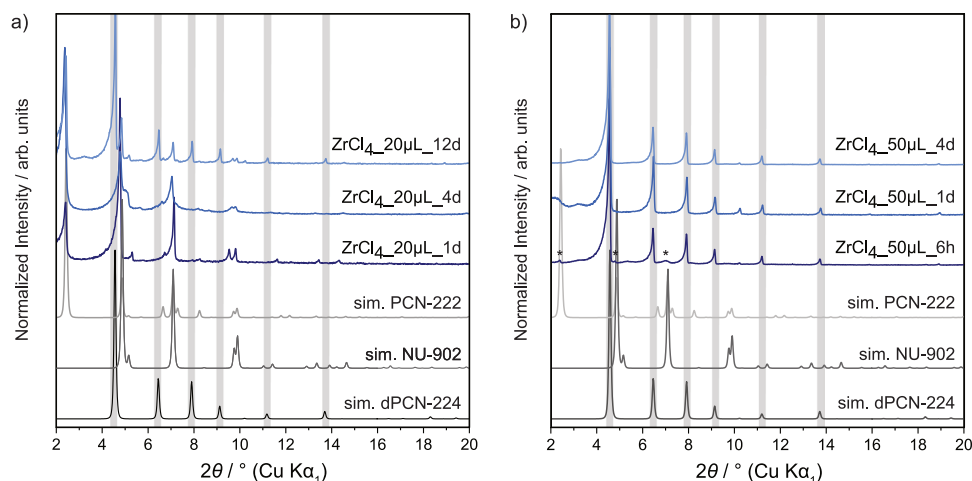

Figure 13. PXRD patterns of the products obtained from ZrCl$_4$_GB under addition of a) 20 µL water after 1-, 4-, and 12-day reaction time and b) 50 µL water after 6-h, 1-, and 4-day reaction time. Peaks corresponding to dPCN-224 are highlighted with grey bars and the asterisks (*) indicates residual PCN-222- or NU-902-like impurities.[18,19d]

**ADVANCED
SCIENCE NEWS**

www.advancedsciencenews.com

**ADVANCED
MATERIALS**

www.advmat.de

3. Conclusion

Our study on dPCN-224 formation from $ZrCl_4$ at difference stages of hydration and hydrolysis shows that its formation follows a complex pathway via at least one intermediate, composed of Zr_6O_8 clusters and TCPP molecules that form anisotropic particles with apparently 1D-ordered chain-like motifs. The intermediate then grows into larger rods, which serve as nucleation surface for dPCN-224. As the reaction progresses, dPCN-224 particles grow into single crystals, consuming the intermediate. Interestingly, hexagonal PCN-222 particles were intermittently obtained as a side product, indicating that the formation of PCN-222 may occur via the same metal–organic intermediate. This work thus illustrates the complex speciation process in Zr–porphyrin MOFs and the variety of Zr–porphyrin-based intermediates formed in the same reaction system as a function of water content. Insights into the local and long-range structure of the formed intermediates further suggests that controlling the reaction conditions can potentially afford novel kinetic products with interesting properties.

In addition, we demonstrate that the Zr source and water content can substantially change the reaction pathway during dPCN-224 formation. Reaction from neat $ZrCl_4$ did not form $Zr_6O_4(OH)_4$ clusters, hence no dPCN-224 was formed. In fact, water is necessary for the formation of $Zr_6O_4(OH)_4$ clusters and should be considered as a reactant during synthesis of dPCN-224. Consequently, the aging time of $ZrCl_4$, and by extension the amount of water present, influences the composition of the obtained product where $Zr_6O_4(OH)_4$ clusters, and ultimately dPCN-224, form faster with increasing water content in the reaction. Whilst hydrolysis of the Zr precursor is key to the formation of a crystalline product, analysis and discussion of the water content during synthesis remains sparse in literature despite its impact on the type of cluster formed, the reaction pathway, and resulting framework. The lack of understanding in this regard is likely the origin of reproducibility issues in literature, highlighting the importance of carefully controlling the environment and history of all reaction ingredients, the reaction itself, and monitoring synthesis with operando tools to provide accurate synthesis protocols. In light of this, our work emphasizes the importance of monitoring the presence of water in both the reagents and environment during MOF crystallization, especially with regards to production scale synthesis, and serves as a general guide to optimize synthetic protocols toward phase-pure porphyrinic Zr-MOFs. Such considerations are likely to be important for a much wider array of MOFs, including all Zr-based MOFs obtained from oxophilic precursors.

4. Experimental Section

Chemicals: TCPP was purchased from Tokio Chemical Industry. Zirconyl chloride octahydrate, zirconium(IV) chloride (anhydrous), benzoic acid, and acetone were purchased from Sigma Aldrich. DMF was purchased from VWR. All chemicals were used as received without further purification.

Synthesis from Different $ZrCl_4$ Sources: Synthesis was carried out from neat $ZrCl_4$ from the glovebox ($ZrCl_4\_GB$), $ZrCl_4\_GB$ that was left in air for 1 day ($ZrCl_4\_GB\_1d$), $ZrCl_4\_GB$ that was left in air for 3 days ($ZrCl_4\_GB\_3d$), and $ZrCl_4$ that was left in air over several months ($ZrCl_4\_lab$). In a typical synthesis, $ZrCl_4$ (120 mg, 0.510 mmol), benzoic acid (1.60 g, 13.1 mmol), and $TCPPH_4$ (40.0 mg, 0.0506 mmol mg) were dissolved in DMF (8 mL) in a 20 mL microwave vial by sonication for 2 min. The mixture was heated in an oven for 24 h at 120 °C. After cooling, the product was collected by centrifugation and washed with DMF (three times, 16 000 rpm/20 min/16 °C) and acetone (twice, 16 000 rpm/8 min/16 °C). The product was soaked in acetone overnight, washed with acetone once, and dried with supercritical CO_2.

Synthesis from $ZrCl_4\_GB$ with Addition of Water: $ZrCl_4\_GB$ (120 mg, 0.510 mmol), benzoic acid (1.60 g, 13.1 mmol), and TCPP (40.0 mg, 0.0506 mmol) were dissolved in DMF (8 mL) in a 20 mL microwave vial by sonication for 2 min. 20 µL (1.1 mmol) or 50 µL (2.8 mmol) of water was added and the mixtures were heated in an oven for 24 h at 120 °C. After cooling, the product was collected by centrifugation and washed with DMF and acetone following the procedure described above. Centrifugation (16 000 rpm/5 min/16 °C) and supercritical CO_2 drying yielded $ZrCl_4\_GB\_20µL$ and $ZrCl_4\_GB\_20µL$ as purple powders.

Time-Dependent Synthesis from $ZrCl_4\_GB$ and $ZrCl_4\_lab$: $ZrCl_4\_GB$ or $ZrCl_4\_lab$ (120 mg, 0.510 mmol), benzoic acid (1.60 g, 13.1 mmol), and TCPP (40.0 mg, 0.0506 mmol) were dissolved in DMF (8 mL) in a 20 mL microwave vial by sonication for 2 min. The mixtures were heated in an oven for varying lengths of time at 120 °C (see Table S2, Supporting Information, for more details). The products were immediately collected by centrifugation, washed with DMF (except of $ZrCl_4\_GB\_2min$, $ZrCl_4\_GB\_1h$, $ZrCl_4\_lab\_2min$) and acetone following the procedure described above and dried with supercritical CO_2.

Time-Dependent Synthesis from $ZrOCl_2·8H_2O$: $ZrOCl_2·8H_2O$ (120 mg, 0.372 mmol), TCPP (40.0 mg, 0.0506 mmol), and benzoic acid (1.30 g, 10.6 mmol) were dissolved in DMF (8 mL) in a 20 mL microwave vial via sonication. The solution was heated in an oven at 120 °C for varying reaction times (see Table S3, Supporting Information, for more details), washed with DMF (three times, 16 000 rpm/15 min/16 °C), and resuspended in DMF (10 mL). The reaction mixture was activated with HCl (8 M, 0.50 mL) in an oven (15 h, 100 °C). The suspension was washed with DMF (twice, 16 000 rpm/20 min/16 °C) and acetone (twice, 16 000 rpm/8 min/16 °C). The mixture was soaked in acetone overnight and washed once with acetone. The product was obtained as purple powder.

Instruments: Ultrasonication was conducted via an ELMASONIC S 100 bath equipped with a high-performance 37 kHz sandwich transducer and state-of-the-art microprocessor. Centrifugation was performed with a benchtop centrifuge Sigma-3-30K from SIGMA. The relative humidity was measured with a Traceable humimeter from VWR.

Microscope Images: Microscope images were taken with a CMOS camera connected to a DM2500 light microscope from LEICA.

Scanning Electron Microscopy: SEM was performed on a Merlin SEM, Zeiss, with a secondary electron detector. The particle sizes were measured with the software ImageJ. For SEM analysis, MOF suspensions were spin-coated onto silicon wafers with a WS-650S-NPP Lite device from LAURELL TECHNOLOGY CORPORATION.

NMR Spectroscopy: ^{1}H-NMR spectra were recorded on a JEOL ECZ 400S 400 MHz spectrometer.

Sorption Measurements: Sorption measurements were acquired on a Quantachrome Instruments Autosorb iQ 3 with nitrogen at 77 K. Samples were activated under high vacuum at 120 °C for 12 h before measurement unless stated otherwise. The pore size distribution was determined from nitrogen adsorption isotherms using the QSDFT (cylindrical pores, adsorption branch) kernel in carbon for nitrogen at 77 K implemented in the ASiQwin software v 3.01.

Thermogravimetric Analysis: Thermogravimetric analysis was performed on a NETZSCH STA 449 F3 Jupiter. Measurements were carried out with 5 mg of sample in an Al_2O_3 crucible under synthetic air flow in a temperature range between 20 and 800 °C and a heating rate of 5 K min^{-1}.

Powder X-Ray Diffraction: PXRD patterns were collected at room temperature on a Stoe Stadi-P diffractometer with Cu-Kα_1 radiation ($\lambda = 1.540596$ Å) or Co-Kα_1 radiation ($\lambda = 1.78896$ Å), a Ge(111) Johann monochromator, and a DECTRIS Mython 1K detector in Debye–Scherrer

geometry. The samples were loaded into 0.5 mm inner diameter glass capillaries and measured over a range of $2\theta = 2.000–30.695°$, with $0.015°$ step size and 50 s counting time per step when using Cu-Kα_1 radiation and a range of $2\theta = 0.500–115.325°$, with $0.015°$ step size and 200 s counting time per step when using Co-Kα_1 radiation.

Rietveld refinements were performed with TOPAS v6.[29] Refinements were performed using a 2θ offset correction, full axial model, and Lorentzian and Gaussian crystallite size broadening convolutions to correct for instrumental and morphological peak-shape effects. The background was described using Chebychev polynomials with a suitable number of terms, typically from 3rd to 11th order, and a One_on_X term to describe increased low angle background scattering. Scale factors, lattice parameters, and an isotropic atomic displacement parameter were refined. Pseudoatoms with a very large atomic displacement parameter were included to describe missing diffuse electron density (to better fit relative intensities of the first few peaks) due to additional water layers located near the cluster surface.[18]

Pair Distribution Function Analysis: Total scattering measurements were carried out using P02.1, the Powder Diffraction, and Total Scattering Beamline, at PETRA III of the German Electron Synchrotron. The rapid acquisition PDF method[30] was used with a large-area 2D PerkinElmer detector (2048×2048 pixels, 200×200 μm^2 each) and sample-to-detector distance of 481.242 mm. The incident energy of the X-rays was 59.795 keV ($\lambda = 0.20735$ Å). Samples were loaded into 0.7 borosilicate or 1 mm inner diameter glass capillaries. An empty capillary was measured as background and subtracted, and a LaB$_6$ standard was measured at room temperature for calibration. Calibration, polarization correction, and azimuthal integration to 1D diffraction patterns were performed using the software pyFAI.[31]

Further correction and normalization of the 1D diffraction intensities were carried out to obtain the total scattering structure function, $F(Q)$, which was Fourier transformed to obtain the PDF, $G(r)$ using PDFgetX3 within xPDFsuite.[32] The maximum Q value used in the Fourier transform of the total scattering data was 20.0 Å^{-1}. A Lorch function was used in the data processing to reduce termination ripples present due to truncation.[33] Simulated PDFs were generated from respective models using Diffpy-CMI.[34]

Electron Diffraction: Electron diffraction data were collected on a Thermo Fisher "Titan" transmission electron microscope operated at 300 kV and at room temperature. Dry polycrystalline powder was gently crushed between two glass slides and transferred onto a continuous-carbon copper grid. The grid was loaded onto a Fischione 2020 tomography holder and inserted into the TEM without further treatment.

Electron beam-defining settings included C2 lens excitation corresponding to spot size number 9 and a C2 aperture of 20 μm. Data collections were conducted using a custom-made script allowing for a stepwise tilt and acquisition of diffraction patterns by a Gatan Ultra Scan 1000 CCD camera. Diffraction data sets were acquired using an oscillation step of $0.25°$ and processed by the software pets2 version 2.1.20211012.1037.[35]

Elemental analysis of carbon, hydrogen, and nitrogen was carried out via an UNICUBE Elementar Analysensysteme GmbH Langenselbold instrument. The zirconium content was determined via ICP-OES using a Vista Pro Simultaneous ICP-OES spectrometer equipped with a CCD detector from Agilent Technologies. The evaluation of the data was conducted using the ICP-Expert software.

Supporting Information

Supporting Information is available from the Wiley Online Library or from the author.

Conflict of Interest

The authors declare no conflict of interest.

Data Availability Statement

The data that support the findings of this study are available from the corresponding author upon reasonable request.

[1] a) G. Kickelbick, M. P. Feth, H. Bertagnolli, M. Puchberger, D. Holzinger, S. Gross, *J. Chem. Soc., Dalton Trans.* **2002**, *20*, 3892; b) G. R. Desiraju, J. J. Vittal, A. Ramanan, *Crystal Engineering: A Textbook*, World Scientific, Singapore **2011**.

[2] a) J. L. C. Rowsell, A. R. Millward, K. S. Park, O. M. Yaghi, *JACS* **2004**, *126*, 5666; b) U. Mueller, M. Schubert, F. Teich, H. Puetter, K. Schierle-Arndt, J. Pastré, *J. Mater. Chem.* **2006**, *16*, 626; c) J. Lee, O. K. Farha, J. Roberts, K. A. Scheidt, S. T. Nguyen, J. T. Hupp, *Chem. Soc. Rev.* **2009**, *38*, 1450; d) Y. Sun, L. Zheng, Y. Yang, X. Qian, T. Fu, X. Li, Z. Yang, H. Yan, C. Cui, W. Tan, *Nano-Micro Lett.* **2020**, *12*, 103.

[3] a) V. V. Butova, A. P. Budnyk, K. M. Charykov, K. S. Vetlitsyna-Novikova, C. Lamberti, A. V. Soldatov, *Chem. Commun.* **2019**, *55*, 901; b) K. McRoberts, W. Zhou, *CrystEngComm* **2021**, *23*, 7658.

[4] T. Islamoglu, K.-I. Otake, P. Li, C. T. Buru, A. W. Peters, I. Akpinar, S. J. Garibay, O. K. Farha, *CrystEngComm* **2018**, *20*, 5913.

[5] M. J. Cliffe, W. Wan, X. Zou, P. A. Chater, A. K. Kleppe, M. G. Tucker, H. Wilhelm, N. P. Funnell, F.-X. Coudert, A. L. Goodwin, *Nat. Commun.* **2014**, *5*, 4176.

[6] a) H. Noh, C.-W. Kung, T. Islamoglu, A. W. Peters, Y. Liao, P. Li, S. J. Garibay, X. Zhang, M. R. DeStefano, J. T. Hupp, O. K. Farha, *Chem. Mater.* **2018**, *30*, 2193; b) T. E. Webber, S. P. Desai, R. L. Combs, S. Bingham, C. C. Lu, R. L. Penn, *Cryst. Growth Des.* **2020**, *20*, 2965; c) P. Li, R. C. Klet, S.-Y. Moon, T. C. Wang, P. Deria, A. W. Peters, B. M. Klahr, H.-J. Park, S. S. Al-Juaid, J. T. Hupp, O. K. Farha, *Chem. Commun.* **2015**, *51*, 10925.

[7] a) F. C. N. Firth, M. W. Gaultois, Y. Wu, J. M. Stratford, D. S. Keeble, C. P. Grey, M. J. Cliffe, *JACS* **2021**, *143*, 19668; b) M. Kløve,

R. S. Christensen, I. G. Nielsen, S. Sommer, M. R. V. Jørgensen, A.-C. Dippel, B. B. Iversen, *Chem. Sci.* **2022**, *13*, 12883.

[8] a) C. McKinstry, E. J. Cussen, A. J. Fletcher, S. V. Patwardhan, J. Sefcik, *Cryst. Growth Des.* **2013**, *13*, 5481; b) D. Salionov, O. O. Semivrazhskaya, N. P. M. Casati, M. Ranocchiari, S. Bjelić, R. Verel, J. A. van Bokhoven, V. L. Sushkevich, *Nat. Commun.* **2022**, *13*, 3762; c) M. L. Kelty, W. Morris, A. T. Gallagher, J. S. Anderson, K. A. Brown, C. A. Mirkin, T. D. Harris, *Chem. Commun.* **2016**, *52*, 7854; d) R. S. Forgan, *Chem. Sci.* **2020**, *11*, 4546; e) A. Schaate, P. Roy, A. Godt, J. Lippke, F. Waltz, M. Wiebcke, P. Behrens, *Chemistry* **2011**, *17*, 6643.

[9] T. E. Webber, W.-G. Liu, S. P. Desai, C. C. Lu, D. G. Truhlar, R. L. Penn, *ACS Appl. Mater. Interfaces* **2017**, *9*, 39342.

[10] a) C. Ardila-Suárez, J. Rodríguez-Pereira, V. G. Baldovino-Medrano, G. E. Ramírez-Caballero, *CrystEngComm* **2019**, *21*, 1407; b) X. Sang, J. Zhang, J. Xiang, J. Cui, L. Zheng, J. Zhang, Z. Wu, Z. Li, G. Mo, Y. Xu, J. Song, C. Liu, X. Tan, T. Luo, B. Zhang, B. Han, *Nat. Commun.* **2017**, *8*, 175; c) G. Zahn, P. Zerner, J. Lippke, F. L. Kempf, S. Lilienthal, C. A. Schröder, A. M. Schneider, P. Behrens, *CrystEngComm* **2014**, *16*, 9198.

[11] F. Ragon, P. Horcajada, H. Chevreau, Y. K. Hwang, U. H. Lee, S. R. Miller, T. Devic, J.-S. Chang, C. Serre, *Inorg. Chem.* **2014**, *53*, 2491.

[12] a) S. M. Shaikh, P. M. Usov, J. Zhu, M. Cai, J. Alatis, A. J. Morris, *Inorg. Chem.* **2019**, *58*, 5145; b) X. Gong, H. Noh, N. C. Gianneschi, O. K. Farha, *J. Am. Chem. Soc.* **2019**, *141*, 6146.

[13] a) W. Morris, B. Volosskiy, S. Demir, F. Gándara, P. L. McGrier, H. Furukawa, D. Cascio, J. F. Stoddart, O. M. Yaghi, *Inorg. Chem.* **2012**, *51*, 6443; b) S. Carrasco, A. Sanz-Marco, B. Martín-Matute, *Organometallics* **2019**, *38*, 3429; c) J. Jin, *New J. Chem.* **2020**, *44*, 15362; d) B. J. Deibert, J. Li, *Chem. Commun.* **2014**, *50*, 9636; e) X. Xie, X. Zhang, M. Xie, L. Xiong, H. Sun, Y. Lu, Q. Mu, M. H. Rummeli, J. Xu, S. Li, J. Zhong, Z. Deng, B. Ma, T. Cheng, W. A. Goddard, Y. Peng, *Nat. Commun.* **2022**, *13*, 63; f) X. Chen, Y. Zhuang, N. Rampal, R. Hewitt, G. Divitini, C. A. O'Keefe, X. Liu, D. J. Whitaker, J. W. Wills, R. Jugdaohsingh, J. J. Powell, H. Yu, C. P. Grey, O. A. Scherman, D. Fairen-Jimenez, *JACS* **2021**, *143*, 13557; g) J. Yang, Z. Wang, Y. Li, Q. Zhuang, W. Zhao, J. Gu, *RSC Adv.* **2016**, *6*, 69807; h) L. Shi, L. Yang, H. Zhang, K. Chang, G. Zhao, T. Kako, J. Ye, *Appl. Catal., B* **2018**, *224*, 60.

[14] a) B. Seoane, S. Castellanos, A. Dikhtiarenko, F. Kapteijn, J. Gascon, *Coord. Chem. Rev.* **2016**, *307*, 147; b) Y. Wu, M. I. Breeze, D. O'Hare, R. I. Walton, *Microporous Mesoporous Mater.* **2017**, *254*, 178; c) C. Zheng, H. F. Greer, C.-Y. Chiang, W. Zhou, *CrystEngComm* **2014**, *16*, 1064.

[15] M. J. Van Vleet, T. Weng, X. Li, J. R. Schmidt, *Chem. Rev.* **2018**, *118*, 3681.

[16] a) F. Millange, M. I. Medina, N. Guillou, G. Férey, K. M. Golden, R. I. Walton, *Angew. Chem., Int. Ed.* **2010**, *49*, 763; b) D. Zacher, J. Liu, K. Huber, R. A. Fischer, *Chem. Commun.* **2009**, *9*, 1031.

[17] X. Liu, S. W. Chee, S. Raj, M. Sawczyk, P. Král, U. Mirsaidov, *Proc. Natl. Acad. Sci. U. S. A.* **2021**, *118*, 2008880118.

[18] C. Koschnick, R. Stäglich, T. Scholz, M. W. Terban, A. von Mankowski, G. Savasci, F. Binder, A. Schökel, M. Etter, J. Nuss, R. Siegel, L. S. Germann, C. Ochsenfeld, R. E. Dinnebier, J. Senker, B. V. Lotsch, *Nat. Commun.* **2021**, *12*, 3099.

[19] a) D. Feng, W.-C. Chung, Z. Wei, Z.-Y. Gu, H.-L. Jiang, Y.-P. Chen, D. J. Darensbourg, H.-C. Zhou, *JACS* **2013**, *135*, 17105; b) D. Feng, Z.-Y. Gu, Y.-P. Chen, J. Park, Z. Wei, Y. Sun, M. Bosch, S. Yuan, H.-C. Zhou, *JACS* **2014**, *136*, 17714; c) P. Deria, D. A. Gómez-Gualdrón, I. Hod, R. Q. Snurr, J. T. Hupp, O. K. Farha, *JACS* **2016**, *138*, 14449; d) D. Feng, Z.-Y. Gu, J.-R. Li, H.-L. Jiang, Z. Wei, H.-C. Zhou, *Angew. Chem., Int. Ed.* **2012**, *51*, 10307; e) H.-L. Jiang, D. Feng, K. Wang, Z.-Y. Gu, Z. Wei, Y.-P. Chen, H.-C. Zhou, *JACS* **2013**, *135*, 13934.

[20] a) K. Epp, A. L. Semrau, M. Cokoja, R. A. Fischer, *ChemCatChem* **2018**, *10*, 3506; b) L. Valenzano, B. Civalleri, S. Chavan, S. Bordiga, M. H. Nilsen, S. Jakobsen, K. P. Lillerud, C. Lamberti, *Chem. Mater.* **2011**, *23*, 1700; c) Y. Bai, Y. Dou, L.-H. Xie, W. Rutledge, J.-R. Li, H.-C. Zhou, *Chem. Soc. Rev.* **2016**, *45*, 2327.

[21] K. S. W. Sing, *Pure Appl. Chem.* **1985**, *57*, 603.

[22] B. Krebs, *Z. Anorg. Allg. Chem.* **1970**, *378*, 263.

[23] R. B. Nevarez, S. M. Balasekaran, E. Kim, P. Weck, F. Poineau, *Acta Crystallogr. C* **2018**, *74*, 307.

[24] Y. Zhang, M. X. Li, M. Y. Lü, R. H. Yang, F. Liu, K. A. Li, *J. Phys. Chem. A* **2005**, *109*, 7442.

[25] A. B. Rudine, B. D. DelFatti, C. C. Wamser, *J. Org. Chem.* **2013**, *78*, 6040.

[26] S. Leubner, R. Siegel, J. Franke, M. T. Wharmby, C. Krebs, H. Reinsch, J. Senker, N. Stock, *Inorg. Chem.* **2020**, *59*, 15250.

[27] a) T. F. Irzhak, V. I. Irzhak, *Dokl. Phys. Chem.* **2019**, *486*, 77; b) V. M. Burlakov, M. S. Bootharaju, T. M. D. Besong, O. M. Bakr, A. Goriely, arXiv:1412.6280, **2014**; c) J. R. Shimpi, D. S. Sidhaye, B. L. V. Prasad, *Langmuir* **2017**, *33*, 9491.

[28] K. Nikoofar, Z. Khademi, *Res. Chem. Intermed.* **2016**, *42*, 3929.

[29] A. Coelho, *J. Appl. Crystallogr.* **2018**, *51*, 210.

[30] P. J. Chupas, X. Qiu, J. C. Hanson, P. L. Lee, C. P. Grey, S. J. L. Billinge, *J. Appl. Crystallogr.* **2003**, *36*, 1342.

[31] a) J. Kieffer, V. Valls, N. Blanc, C. Hennig, *J. Synchrotron Radiat.* **2020**, *27*, 558; b) G. Ashiotis, A. Deschildre, Z. Nawaz, J. P. Wright, D. Karkoulis, F. E. Picca, J. Kieffer, *J. Appl. Crystallogr.* **2015**, *48*, 510.

[32] a) P. Juhas, T. Davis, C. L. Farrow, S. J. L. Billinge, *J. Appl. Crystallogr.* **2013**, *46*, 560; b) X. A. J. Yang, J. Pavol, C. L. Farrow, S. J. L. Billinge, arXiv:1402.3163, **2014**; c) S. J. L. Billinge, C. L. Farrow, *J. Phys.: Condens. Matter* **2013**, *25*, 454202.

[33] E. Lorch, *J. Phys.: Condens. Matter* **1969**, *2*, 229.

[34] P. Juhas, C. L. Farrow, X. Yang, K. R. Knox, S. J. L. Billinge, *Acta Crystallogr. A* **2015**, *71*, 562.

[35] L. Palatinus, *PETS-Program for Analysis Electron Diffraction Data*, Institute of Physics of the AS CR, Prague, Czechia **2011**.